Entropy of ultrasound-contrast-agent velocity fields for angiogenesis imaging in prostate cancer

Entropy of Ultrasound-Contrast-Agent Velocity Fields for Angiogenesis Imaging in Prostate Cancer

Ruud JG van Sloun,* Libertario Demi, Arnoud W Postema, Jean JMCH De La Rosette, Hessel Wijkstra, and Massimo Mischi

***Abstract*— Prostate cancer care can benefit from accurate and cost-efficient imaging modalities that are able to reveal prognostic indicators for cancer. Angiogenesis is known to play a central role in the growth of tumors towards a metastatic or a lethal phenotype. With the aim of localizing angiogenic activity in a non-invasive manner, Dynamic Contrast Enhanced Ultrasound (DCE-US) has been widely used. Usually, the passage of ultrasound contrast agents thought the organ of interest is analyzed for the assessment of tissue perfusion. However, the heterogeneous nature of blood flow in angiogenic vasculature hampers the diagnostic effectiveness of perfusion parameters. In this regard, quantification of the heterogeneity of flow may provide a relevant additional feature for localizing angiogenesis. Statistics based on flow magnitude as well as its orientation can be exploited for this purpose. In this paper, we estimate the microbubble velocity fields from a standard bolus injection and provide a first statistical characterization by performing a spatial entropy analysis. By testing the method on 24 patients with biopsy-proven prostate cancer, we show that the proposed method can be applied effectively to clinically acquired DCE-US data. The method permits estimation of the in-plane flow vector fields and their local intricacy, and yields promising results (receiver-operating-characteristic curve area of 0.85) for the detection of prostate cancer.**

***Index Terms*— Cancer, entropy, medical diagnostic imaging, ultrasonic imaging.**

I. Introduction

PROSTATE cancer (PCa) is the second-leading cause of cancer death in men, and the most frequently diagnosed cancer in men aside from skin cancer [1]. PCa diagnosis is typically performed using systematic needle biopsies, guided by transrectal ultrasound (TRUS): the extraction and examination of prostate gland samples based on a standard template. The samples are microscopically assessed based on the histopathological degree of cell differentiation, quantified by the Gleason score [2]. In this case, TRUS is merely used to guide the biopsy needle. Despite being the current golden standard, initial systematic biopsies miss nearly a quarter of the clinically significant cancers [3], requiring additional biopsy sessions in case of suspicion. To enhance tumor detection rates, targeting of biopsies using multi-parameteric magnetic resonance imaging (mpMRI) [4], [5] has been proposed. This strategy combines T2 weighted and Diffusion weighted imaging with Dynamic Contrast Enhanced MRI (DCE-MRI) to detect and classify lesions, which can be targeted specifically during the biopsy procedure. Besides enabling targeted biopsies, accurate delineation of lesions using imaging would permit the use minimally invasive therapies such as focal therapy as opposed to radical prostatectomy. Nevertheless, mpMRI is a modality with high costs and a complex workflow. It would therefore be favorable to perform these diagnostic strategies by cost-effective TRUS.

Dynamic Contrast Enhanced Ultrasound (DCE-US) is a minimally invasive imaging modality that can be applied using TRUS. Where DCE-MRI in mpMRI is mainly used to assess microvascular permeability, DCE-US is used to analyze perfusion, by imaging an intravenously injected cloud of contrast agents that remain intra-vascular. In the context of tumor detection, a particularly interesting application of DCE-US concerns the localization of neo-angiogenic vascularization associated with tumor growth and metastasis [6]–[8], and of lethal phenotypes [9].

The microvascular network that originates from tumor-driven angiogenesis is characterized by increased microvascular density (MVD) and tortuosity, as well as by the presence of irregular branching and arteriovenous shunts. Decreasing functional vascular cross-sectional area in neoplastic tissue can increase flow resistance. Hypoxia in tumors due to ineffective blood flow can lead to deteriorated endothelial wall cells, causing extra-vascular leakage and metastases [10]. These factors contribute to heterogeneous blood flow in angiogenic vasculature [11], [12]. In this paper, we aim at localizing tumor-driven angiogenesis by exploiting the heterogeneity induced in the microvascular blood flow.

Focusing on increased microvascular density, several researchers have studied DCE-US time-intensity features related to microvascular perfusion [13]–[15]. However,

Manuscript received October 6, 2016; revised November 9, 2016; accepted November 13, 2016. Date of publication November 16, 2016; date of current version March 2, 2017. This work is part of the research programme 10769, which is partly financed by the Netherlands Organisation for Scientific Research (NWO). The research has also received funding from the European Research Council / ERC grant agreement n. 280209. *Asterisk indicates corresponding author.*

*R. JG van Sloun is with the Lab. of Biomedical Diagnostics, Eindhoven University of Technology, Eindhoven 5612 AZ, The Netherlands (e-mail: r.j.g.v.sloun@tue.nl).

L. Demi and M. Mischi are with the Lab. of Biomedical Diagnostics, Eindhoven University of Technology, Eindhoven 5612 AZ, The Netherlands.

A. W Postema W and J. JMCH De La Rosette are with the Academical Medical Center University Hospital, Amsterdam 1105 AZ, The Netherlands.

H. Wijkstra is with the Lab. of Biomedical Diagnostics, Eindhoven University of Technology, Eindhoven 5612 AZ, The Netherlands and also with Academical Medical Center University Hospital, Amsterdam, The Netherlands.

Digital Object Identifier 10.1109/TMI.2016.2629851

ultrasound attenuation and scanner settings may affect the estimation of local contrast-agent concentration and the resulting amplitude-based perfusion parameters [16]–[18]. Moreover, its effectiveness is hampered by the heterogeneous nature of blood flow in angiogenesis. Exploiting this, intra-tumor vascular heterogeneity has been assessed for DCE-CT [19] and DCE-MRI [20]. In the domain of ultrasound, a histogram-based characterization of contrast agent wash-in rate distributions was used to classify benign or malignant ROIs [21]. Later, a DCE-US perfusion clustering algorithm was developed for the assessment of perfusion heterogeneity [22]. As an alternative to perfusion related parameters, features linked to contrast agent bolus dispersion have been proposed [23], [24]. These approaches are based on the hypothesis that structural alterations in the vascular architecture result in variations in contrast agent spreading: a macroscopic perspective of vascular characterization that is connected to modeling of flow through porous media [25], [26].

Additionally, disruption-replenishment techniques were investigated for vascular characterization [27]. After disrupting all microbubbles with a high-intensity flash, re-perfusion kinetics are assessed by extracting parameters related to vascular cross-sectional area, mean flow speed, and vascular heterogeneity of the microvasculature using a log-normal model for the spatial flow distribution. Such approaches require the use of a destructive flash along with a steady infusion of contrast agents, and quantification depends on the angle between the imaging beam and the replenishing vessels [28].

In this work, we infer vascular heterogeneity by providing a bivariate statistical characterization of flow including contrast agent directionality. To this end, we first measure the ultrasound contrast agent's (UCA) indicator dilution curves (IDCs; a measure of contrast agent concentration over time) that result from an intravenous bolus injection at each pixel. From this, we estimate the local propagation vector of the agent's distribution over space. By estimating the time-delays between the IDCs measured at a set of imaging pixels, the macroscopic flow direction as well as its magnitude can be estimated. The diversity or disorder of the resulting vector field is then assessed by evaluating Shannon's Entropy [29], [30], ultimately yielding a measure of heterogeneity. Its diagnostic value is evaluated on data acquired from 24 patients and compared against histology.

The remainder of this paper is organized as follows. We first describe the data acquisition protocol (Secs. II-A-II-C). A velocity vector field estimator is then derived based on a two-stage cross-correlation/least squares approach (Sec. II-E). Next, two approaches for statistical characterization based on Entropy (Sec. II-F) and Conditional Entropy (Sec. II-G) are proposed. The adopted validation methodology is reported in Sec. III, and the results are presented in Sec. IV. Finally, in Sec. V, the results are discussed and conclusions derived.

II. Methods

A. Patient Population

Initially, twenty-five patients scheduled for radical prostatectomy where included in this study. DCE-US investigations were performed on all patients. One patient was excluded based on unreliable histological data, compromising the validation procedure. The study was approved by the local ethics committee. All patients signed informed consent.

B. DCE-US Data Acquisition

The DCE-US data were acquired at the AMC University Hospital (Amsterdam, the Netherlands). An intravenous injection of a 2.4-ml UCA bolus (SonoVue ®, Bracco, Milan, Italy) was administered, and its passage through the prostate was imaged using a C10-3v transrectal endfiring ultrasound probe. The DCE-US loops were acquired and stored using a Philips iU22 ultrasound system (Philips Healthcare, Bothell, WA), operating in a contrast-specific imaging mode. This mode exploits the microbubble's nonlinear behavior using a power modulation pulse scheme at 3.5 MHz to suppress linear backscattering from tissue. A low mechanical index of 0.06 was used to minimize microbubble destruction [31]. The frame rate was 10 Hz. The axial resolution of the ultrasound system is approximately 0.3 mm and its lateral resolution is in the order of 0.5 mm at 5 cm from the probe. At this distance, the elevational beamwidth is approximately 3.4 mm. The pixel spacing is 0.146 mm in both directions. The median number of DCE-US planes recorded per patient was 2, ranging between 1 and 4. Imaging was performed for 120 seconds to record the full in- and out flow.

C. Histopathological Analysis

A radical prostatectomy was performed in all patients. After resection, the prostate specimen was fixed in formalin, and dissected in 4-mm-thick slices. The slices were Haematoxylin & Eosin stained, and a pathologist determined the presence and extent of the tumor, based on the level of cell differentiation, according to [32]. Six patients had a Gleason score of $3+3=6$, nine patients had a Gleason score of $3+4=7$, five patients had a Gleason score of $4+3=7$, one patient had a Gleason score of $3+5=8$, one patient had a Gleason score of $4+5=9$, and two patients had a Gleason score of $5+4=9$.

D. Pre-Processing

Prior to the analysis, the recorded log-compressed and quantized time-intensity curves were linearized to obtain IDCs using the methods described in [23]. A spatial Gaussian filter with a standard deviation of one pixel (0.146 mm) was then applied to mitigate the impact of spatially incoherent noise [33].

E. Velocity Vector Field Estimation

For the purpose of estimating the in-plane UCA velocity vector at a certain location, we consider the IDCs that are measured at a specific set of imaging pixels around this location: N pixels distributed on a circle with radius R. The IDC shapes of two closely spaced pixels (<2.2 mm) are similar since local effects are dominated by the complete UCA bolus history. Hence, assuming the transport of UCAs between two distinct pixels in this set to be convection-dominated, the measured IDCs may be written as:

$$y_1(t) = u_1(t)s(t) + n_1(t) \tag{1}$$

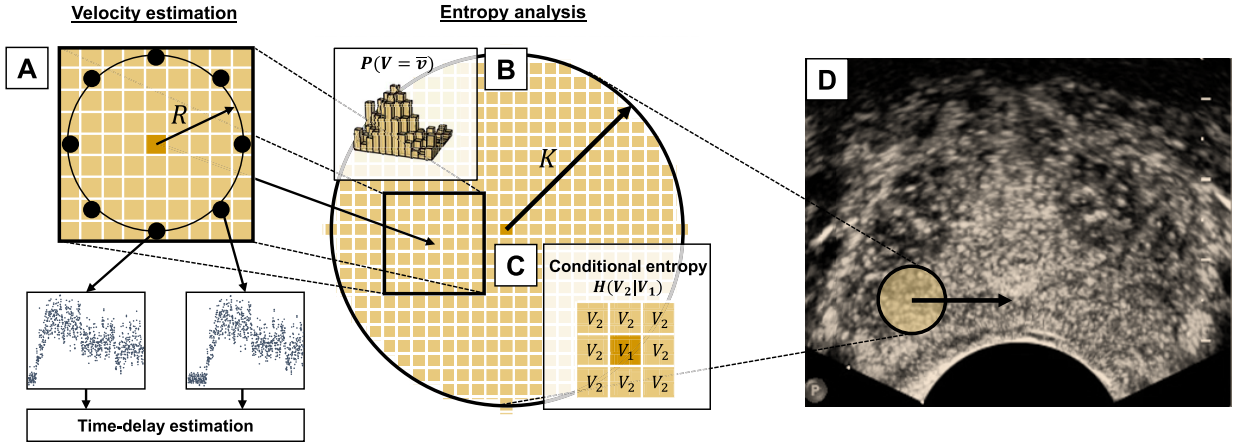

Fig. 1. An illustration of the analysis steps: First, the velocity vector is estimated for all pixels based on IDC time-delay estimation (A). Then, its bivariate probability distribution is estimated within a kernel to derive the entropy (B). Finally, the conditional entropy is determined (C), and the kernel is translated across imaging plane (D).

$$y_2(t) = u_2(t)s(t-\tau) + n_2(t), \tag{2}$$

where $s(t)$ represents the time evolution of contrast signal, τ is its time-delay with respect to the arrival time at the first pixel, $n_1(t)$, $n_2(t)$ are i.i.d additive noise components, and $u_1(t)$, $u_2(t)$ are i.i.d multiplicative noise components. The additive noise components model e.g. thermal and electronic noise, whereas the multiplicative components can describe the effects of speckle noise on the measured IDCs ([34], [35]). The time-delay τ can be estimated by maximizing the cross-correlation function between $y_1(t)$ and $y_2(t)$, i.e.

$$\begin{aligned}\hat{\tau}_{1,2} &= \arg\max_{\tilde{\tau}} E\left[y_1(t)y_2(t+\tilde{\tau})\right] \\ &= \arg\max_{\tilde{\tau}} \{E\left[u_1(t)u_2(t)s(t)s(t-\tau+\tilde{\tau})\right] \\ &\quad + E\left[u_2(t)n_1(t)s(t-\tau+\tilde{\tau})\right] + E\left[u_1(t)n_2(t)s(t)\right] \\ &\quad + E\left[n_1(t)n_2(t)\right]\} \\ &= \arg\max_{\tilde{\tau}} E\left[s(t)s(t-\tau+\tilde{\tau})\right], \end{aligned} \tag{3}$$

where $E\{\cdot\}$ is the expectation operator. This function is maximized for $\tau = \tilde{\tau}$ [36]. Analogous to the convolution theorem, the cross-correlation based time-delay estimation can also be performed using the Fourier transform, via:

$$\hat{\tau}_{1,2} = \arg\max_{\tilde{\tau}} \int_{-\infty}^{\infty} Y_1(\omega)Y_2^*(\omega)e^{-j\omega\tilde{\tau}}d\omega, \tag{4}$$

where $Y_1(\omega)$ and $Y_2(\omega)$ are the Fourier transforms of $y_1(t)$ and $y_2(t)$, respectively, and $(\cdot)^*$ denotes the complex conjugate. In practice, this allows us to pre-compute and store the Fast Fourier Transforms (FFTs) of all IDCs, reducing the procedure's computation time by avoiding duplicate FFT evaluations while translating the ring-kernel (see Figure 1). We then collect all the $N(N-1)$ time-delays amongst all the IDCs from the set in an array $\hat{\vec{\tau}}$. The relation between $\hat{\vec{\tau}}$ and the average velocity vector $\vec{v}$ can be described as:

$$\vec{v}^T\hat{\vec{\tau}} = \mathrm{D}, \tag{5}$$

where D is the $2 \times N(N-1)/2$ matrix that describes the inter-pixel distance vectors. Equation (5) is solved for $\vec{v}$ by minimizing the mean squared error between $\vec{v}^T\hat{\vec{\tau}}$ and D using weighted least-squares minimization:

$$\hat{\vec{v}} = \arg\min_{\vec{v}} \sum_{i}^{N(N-1)} w_i \left|\mathrm{D}_i - \vec{v}\hat{\tau}_i\right|_2^2, \tag{6}$$

where D_i is the i^{th} column of D and $\hat{\tau}_i$ is the corresponding time delay. The weight w_i is the value of the normalized cross-correlation function at lag $\hat{\tau}_i$, reflecting our confidence in the time-delay estimate:

$$w_i = \frac{E\left[y_{i,1}(t)y_{i,2}(t+\hat{\tau}_i)\right]}{\sigma_{y_{i,1}}\sigma_{y_{i,2}}}, \tag{7}$$

where $\sigma_{y_{i,1}}$ and $\sigma_{y_{i,2}}$ depict the standard deviations of $y_{i,1}$ and $y_{i,2}$, respectively.

This procedure is repeated on a grid of pixels that covers the prostate to produce an estimate of the complete vector field. An *in silico* validation of the velocity vector field estimator is given in appendix A.

F. Entropy

To locally assess the amount of diversity or disorder in the field components we calculate its Shannon's entropy [30]. This information theoretical quantity provides a measure of the intricacy of the velocity field pattern: the higher the heterogeneity the higher the entropy. Shannon's entropy is defined as

$$H(V) = -\int \mathrm{P}(\vec{v})\log\mathrm{P}(\vec{v})d\vec{v}. \tag{8}$$

where $\mathrm{P}(\vec{v} = [v_x, v_y])$ is the two-dimensional probability distribution for the occurrence of a specific velocity vector (x and y components) and log denotes the natural logarithm.

Since $\mathrm{P}(\vec{v})$ is unknown, we estimate its discrete probability mass function from the data based on rectangular bins, by computing the two-dimensional histogram $\tilde{\mathrm{P}}(i, j)$ of all the

velocity vectors obtained within a circular kernel of radius K (see Figure 1), i.e.,

$$\tilde{\mathrm{P}}(i,j) = \tilde{\mathrm{P}}(V \in \mathrm{bin}\{i,j\}) = \frac{1}{|\mathcal{S}_k|} \sum_{m \in \mathcal{S}_K} c(\vec{v}_m, i, j), \tag{9}$$

where $\mathcal{S}_K$ is the set of indices that point to the velocity vectors in the kernel, $\vec{v}_m$ is the m^{th} velocity vector, and the bin function

$$c(\vec{v}_m, i, j) = \begin{cases} 1 & \text{if } \vec{v}_m \in \mathrm{bin}\{i,j\} \\ 0 & \text{otherwise} \end{cases}, \tag{10}$$

where the rectangular bin width is $2v_{max}/N_b$, with N_b being the amount of bins in both dimensions and v_{max} the upper limit of the velocity magnitude. The entropy is then estimated from the data as:

$$\hat{H}(V) = -\sum_{i,j} \tilde{\mathrm{P}}(i,j) \log \tilde{\mathrm{P}}(i,j). \tag{11}$$

G. Conditional Entropy

To extend the analysis of spatial heterogeneity, we consider the predictive value of a velocity vector with respect to its surrounding pixels. We describe this with the conditional entropy of the field given knowledge about its direct neighborhood. To this end, we employ the conditional probability density function of a specific velocity vector at a certain location (described by random variable V_1) given a neighboring velocity vector (V_2):

$$\begin{aligned} H(V_2|V_1) &= \int \mathrm{P}(\vec{v_1}, \vec{v_2}) \log \frac{\mathrm{P}(\vec{v_1})}{\mathrm{P}(\vec{v_1}, \vec{v_2})} d\vec{v}_1 d\vec{v}_2 \\ &= \int \mathrm{P}(\vec{v_2}|\vec{v_1})\mathrm{P}(\vec{v_1}) \log \frac{\mathrm{P}(\vec{v_1})}{\mathrm{P}(\vec{v_2}|\vec{v_1})\mathrm{P}(\vec{v_1})} d\vec{v}_1 d\vec{v}_2 \\ &= -\int \mathrm{P}(\vec{v_1}) \int \mathrm{P}(\vec{v_2}|\vec{v_1}) \log \mathrm{P}(\vec{v_2}|\vec{v_1}) d\vec{v}_2 d\vec{v}_1. \end{aligned} \tag{12}$$

The conditional entropy $H(V_2|V_1)$ is equal to zero if V_1 is completely determined by V_2.

Again, the true probability density functions are inherently unknown. Hence, we compute their discrete probability mass function estimates $\tilde{\mathrm{P}}(V_1 \in \mathrm{bin}\{i,j\})$ and $\tilde{\mathrm{P}}(V_2 \in \mathrm{bin}\{k,l\}|V_1 \in \mathrm{bin}\{i,j\})$ according to (9), using the data obtained within a circular kernel of radius K based on two-dimensional histograms. Similarly, the conditional probability distribution can be estimated as:

$$\begin{aligned} \tilde{\mathrm{P}}(k,l|i,j) &= \tilde{\mathrm{P}}(V_2 \in \mathrm{bin}\{k,l\}|V_1 \in \mathrm{bin}\{i,j\}) \\ &= \frac{\frac{1}{|\mathcal{S}_k|} \sum_{m \in \mathcal{S}_K} \frac{1}{|\mathcal{S}_m|} \sum_{n \in \mathcal{S}_m} c(\vec{v}_m, i, j) c(\vec{v}_n, k, l)}{\frac{1}{|\mathcal{S}_k|} \sum_{m \in \mathcal{S}_K} c(\vec{v}_m, i, j)}, \end{aligned} \tag{13}$$

where $\mathcal{S}_m$ is the set of indices that point to the velocity vectors that lie adjacent to the m^{th} velocity vector. The conditional entropy is then calculated as:

$$\hat{H}(V_2|V_1) = \sum_{i,j} \tilde{\mathrm{P}}(i,j) \sum_{k,l} \tilde{\mathrm{P}}(k,l|i,j) \log \tilde{\mathrm{P}}(k,l|i,j). \tag{14}$$

The analysis is repeated by sliding the circular kernel across the entire vector field in order to generate parametric maps of $\hat{H}(V)$ and $\hat{H}(V_2|V_1)$.

An illustrative overview of the described methodology is shown in Figure 1.

III. Validation Methodology

The proposed method was clinically validated on a group of twenty-four patients, of which fifty-seven DCE-US planes were included. Contrast-mode as well as fundamental-mode loops were simultaneously recorded for each plane. Additional fundamental-mode US sweeps were recorded from the prostate's base to apex for each patient. These served as a reference for manual identification of the DCE-US plane location within the full prostate volume using the anatomical features captured by the fundamental mode images. Then, cognitive registration between the histopathological set of slices with marked lesions and the DCE-US planes permitted drawing regions of interest (ROIs) of approximately 0.5 cm^2 indicating either benign (Gleason score $< 3+3 = 6$) or malignant areas. For this purpose, fundamental mode (B-mode) sweep videos ranging from base to apex where acquired. By comparing this video with the fundamental mode image obtained in the contrast imaging plane, the contrast imaging plane location was determined. Then the corresponding histology slice was chosen.

To mitigate errors in the registration procedure, slices with small tumors (with respect to the ROIs) and inconsistencies across multiple slices were not considered suitable for drawing malignant ROIs. In total, fifty-two benign regions and fifty-tree malignant ROIs were selected. On average, these ROIs included about 2000 time-intensity curves (min: 308, max: 6695), and were drawn prior to the development of the methods presented in this work.

A Receiver-Operating-Characteristic (ROC) analysis was adopted to evaluate classification performance: Pixel-based classification was performed using a variable threshold per parameter, thereby displaying the relation between sensitivity and specificity in a curve. The area under the ROC curve is used as a general measure of flexibility and performance. The optimal classification threshold is a trade-off between sensitivity and specificity, and was determined by selecting the point on the ROC curve that yields the minimum Euclidean distance to ideal classification, *i.e.* to a sensitivity and specificity of 1. The method's sensitivity, specificity, positive predictive value, and negative predictive value were calculated for this threshold.

The adopted algorithm settings are given in Table I. The number of pixels in the ring kernel for velocity estimation N was set to 8; a trade-off between inter-pixel spacing (related to the system resolution) and least-squares estimation variance. The entropy kernel radius K was set to 3.6 mm, being a trade-off between the accuracy of the probability density estimates and the achieved spatial resolution of the parametric maps. v_{max} was set to 1 mm/s, in line with the expected blood velocities in human capillaries [37]. The method's performance was assessed for 3 different radii of the velocity estimation

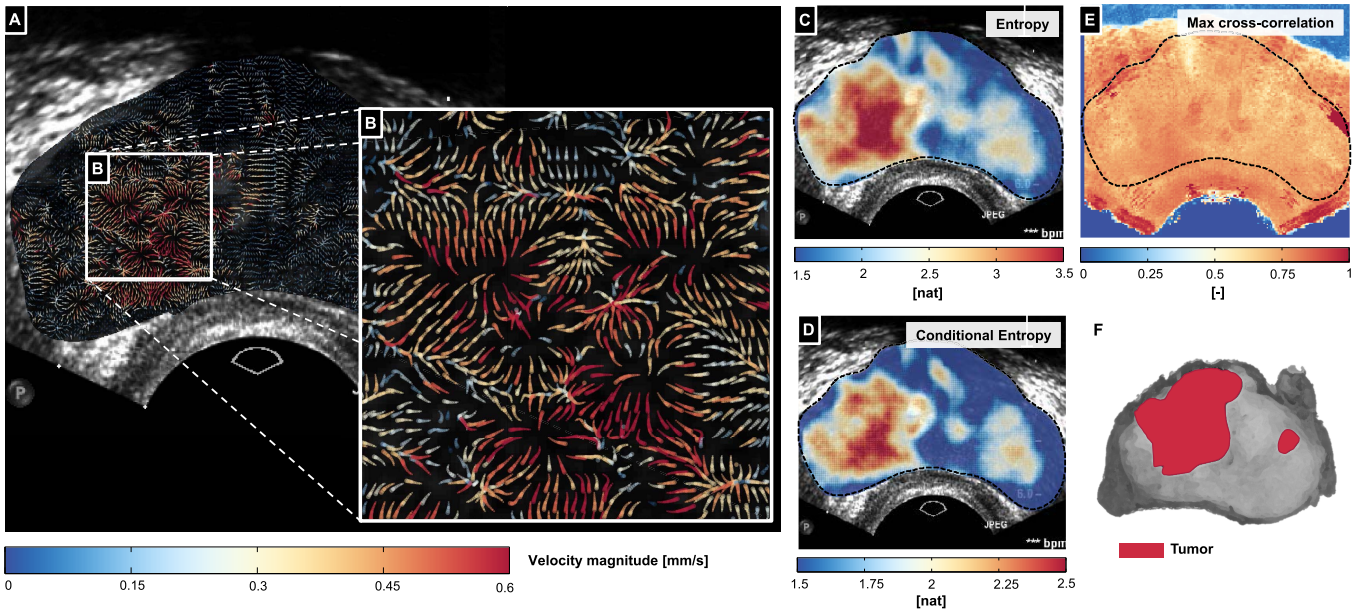

Fig. 2. An example of the estimated ultrasound-contrast-agent velocity fields (A, zoom B), as well as the parametric maps resulting from the statical characterization using Entropy (C) and Conditional Entropy (D). Image values are given in nats (natural unit of information). To provide a measure of confidence in the time-delay estimation procedure, a map of the maximum normalized cross-correlation values is shown in (E). The corresponding histology slice is also given (F). Tumor lesions are marked in red.

TABLE I
ADOPTED SETTINGS FOR THE PROPOSED ALGORITHM. VALUES BETWEEN BRACKETS INDICATE THE SET OF TESTED PARAMETERS

Parameter	Description	Value
N	Pixels in set of velocity estimation	8
K	Kernel radius for entropy analysis	3.6 mm
v_{max}	Maximum histogram bin velocity	1 mm/s
R	Radius circle for velocity estimation	{0.7,0.9,1.2} mm
N_b	Histogram bins	{9,12,15}

kernel R, and varying number histogram bins.

The pixel-wise signal quality was assessed by estimating the Signal to Noise Ratio (SNR). The signal component $s[n]$ was estimated by filtering the TIC with a moving median filter (window size of 4 seconds) and subtracting the baseline, which was estimated by calculating the median value in the first 5 seconds of the TIC. The noise component $u[n]$ was estimated by subtracting the filtered TIC from the raw TIC. A measure of SNR in dB is then calculated as:

$$\text{SNR} = 10\log_{10}\left(\frac{\sum_n s[n]^2}{\sum_n (u[n]-\bar{u})^2}\right), \tag{15}$$

where $\bar{u}$ is the mean value of u across all samples.

The classification performance of the proposed methods was compared to that obtained with different DCE-US quantification parameters reported in the literature. To this end, the spatiotemporal correlation (r) [24], wash-in time (WIT) [38], wash-in rate (WIR), peak intensity (PI), and area under the IDC (AUC) were also extracted. To facilitate a robust estimation process, the Local Density Random Walk model was fitted to the curves according to [23], after which the desired parameters could be derived.

Additionally, a comparison amongst heterogeneity-based measures was made by evaluating the classification performance obtained by estimating the entropy of the other quantification parameters based on a univariate version of the methods described in Sec. II-F

To achieve similar spatial smoothing as the kernel-based entropy analysis, the single-pixel parameters were post-filtered using a 2D Gaussian kernel (standard deviation of 1.3 mm, half the entropy kernel radius).

Finally, the p-values for testing the hypothesis that there is a difference between the parameter means for benign and malignant areas were calculated. Since some of the parameter distributions are heavily skewed and do not follow a normal distribution, a non-parametric Kruskal-Wallis test (one-way ANOVA on ranks) was adopted for this purpose [39]. Taking into account the spatial correlation between parameter values within a ROI, the number of independent samples in a distribution was conservatively set to the number of ROIs used for that distribution.

IV. RESULTS

Figure 2 shows a qualitative example of the obtained velocity fields, along with the parametric maps of its Entropy and Conditional Entropy. In addition, the maximum normalized cross-correlation value (i.e. weight, see Eqn. (7)) is given for each pixel, serving as a measure of confidence in the velocity estimate. The corresponding histology slice is also shown. One can observe that both parameters display elevated values in areas with marked tumor lesions.

Figure 3 shows two typical examples of the probability density function estimates of the velocity fields within a kernel from a benign and malignant region. One can observe a broad

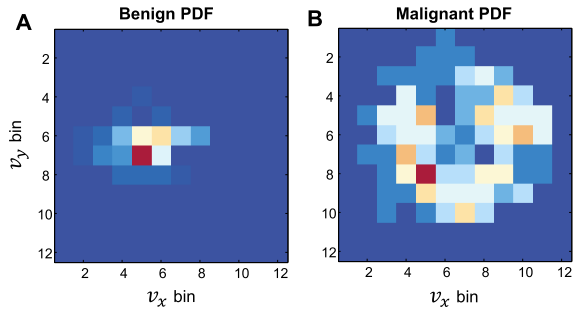

Fig. 3. Typical probability density function estimates of velocity fields from benign (A) and malignant (B) regions.

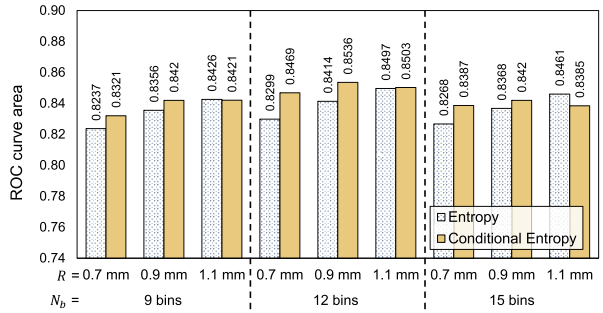

Fig. 4. Description of performance in terms of Receiver-Operating-Characteristics curve area (range 0-1), as a function of algorithm settings. Blue dotted bars indicate the performance for Entropy, yellow bars give the performance for Conditional Entropy.

distribution of velocity vectors in the malignant case, resulting in a high entropy.

Figure 4 displays the attained ROC curve areas for the velocity field Entropy as well as the velocity field Conditional Entropy as a function of the radius R and the number of histogram bins N_b. The adopted settings are summarized in Table I. One can observe that the highest ROC curve area is reached with $R = 1.1$ mm and $N_b = 12$ for Entropy, and $R = 0.9$ mm and $N_b = 12$ for Conditional Entropy. For the remainder of the results, the adopted settings are $R = 0.9$ mm and $N_b = 12$, unless explicitly mentioned otherwise.

Figure 5 demonstrates the relation between the achieved ROC curve areas of the proposed methods and measurement quality in terms of SNR. Performance monotonically increases when excluding pixels from the ROIs based on SNR. As a consequence, the number of independent samples decreases. To provide an indication of this reduction in data, the amount of benign and malignant ROIs that preserve over 50% of their pixels after exclusion is also plotted.

The histograms and box-plots of the benign and malignant classes for velocity field Entropy and Conditional Entropy are given in Figure 6. The malignant class distribution displays higher median values for both parameters. Moreover, the box-plots indicate that the 25th percentile ($Q1$) of the malignant distribution is higher than the 75th percentile ($Q3$) of the benign distribution for both parameters. Values are depicted as outliers if they are larger than $Q3 + 1.5(Q3 - Q1)$ or smaller than $Q1 - 1.5(Q3 - Q1)$. A pixel was classified malignant for Entropy > 2.47 and Conditional Entropy > 1.91.

In Figure 7, two typical parametric maps of velocity-field Conditional Entropy are shown together with their binary

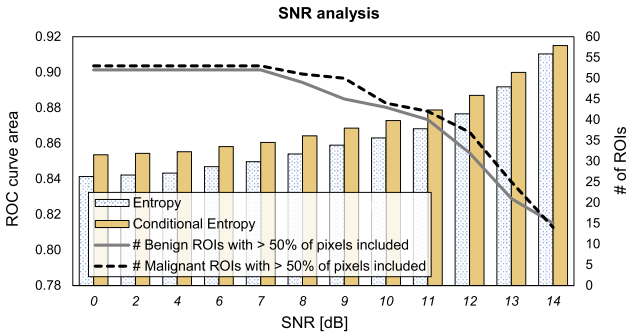

Fig. 5. Description of performance in terms of Receiver-Operating-Characteristics curve area (range 0-1), as a function of SNR threshold. Blue dotted bars indicate the performance for Entropy, yellow bars give the performance for Conditional Entropy (R=0.9 mm, N_b=12 bins). The amount of benign and malignant ROIs that preserve over 50% of their pixels after applying the SNR threshold are given by the solid grey and dashed black lines, respectively.

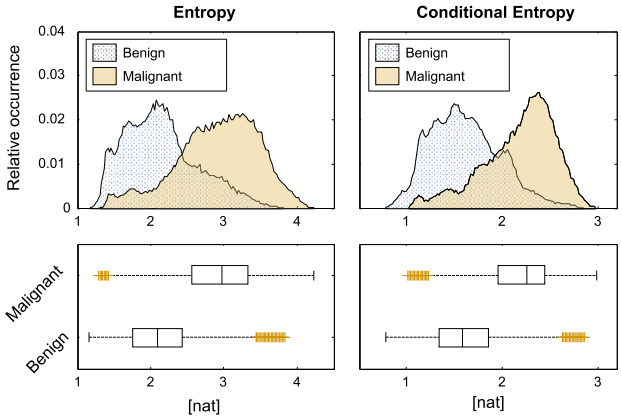

Fig. 6. The benign (blue dotted) and malignant (yellow) class histograms for Entropy and Conditional Entropy (R=0.9 mm, N_b=12 bins). A pixel was classified malignant for Entropy > 2.47 and Conditional Entropy > 1.91. The corresponding box-plots for both classes are also given. Outliers are indicted with yellow crosses.

classification maps obtained by applying the histogram-based optimal threshold. The adopted benign and malignant ROIs are displayed, as well as the resulting classification performance within the ROIs as described in Sec. III. For comparison the corresponding parametric maps of AUC, PI, WIR and WIT are also given.

Figure 8 shows the ROC curves for velocity field Entropy and Conditional Entropy along with those obtained using other entropy and non-entropy based DCE-US quantification methods. The classification characteristics of Conditional Entropy generally yield higher specificities, whereas Entropy tends to result in higher sensitivities. Both methods outperform the reference quantification methods.

The pixel-based classification results are summarized in Table II, where the settings that yield the highest ROC curve area for velocity field Entropy and Conditional Entropy (see Figure 4) are used. Of all evaluated parameters, Conditional Entropy yields the highest ROC curve area. The difference with respect to Entropy is however small. The AUC yields the lowest ROC curve area, and the lowest values of sensitivity, specificity, negative predictive value, and positive

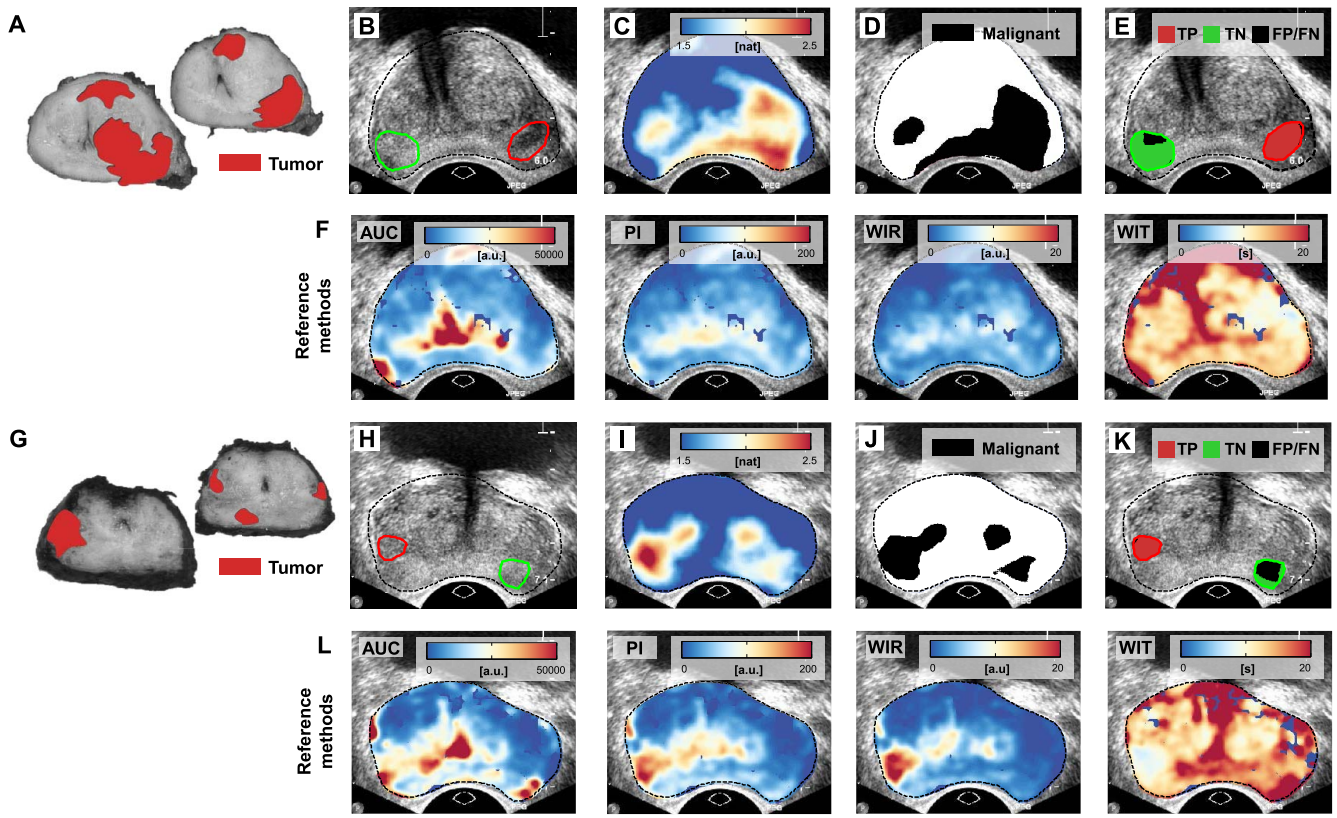

Fig. 7. Two examples of benign and malignant regions of interest (ROIs, as defined in section III) drawn on the fundamental mode images (B,H), along with the nearest histology slices (A,G). The maps of conditional entropy for these imaging planes are shown in (C,I). Classification results using the pixel-based optimal threshold are given in (D,J) for the full field of view. Finally, the true positives (green), true negatives (red), and false positives/negatives (black) are shown in (E,K). As a reference, the maps of area under the IDC (AUC), peak-intensity (PI), wash-in time (WIT), and wash-in rate (WIR) for these imaging planes are given in (F,L).

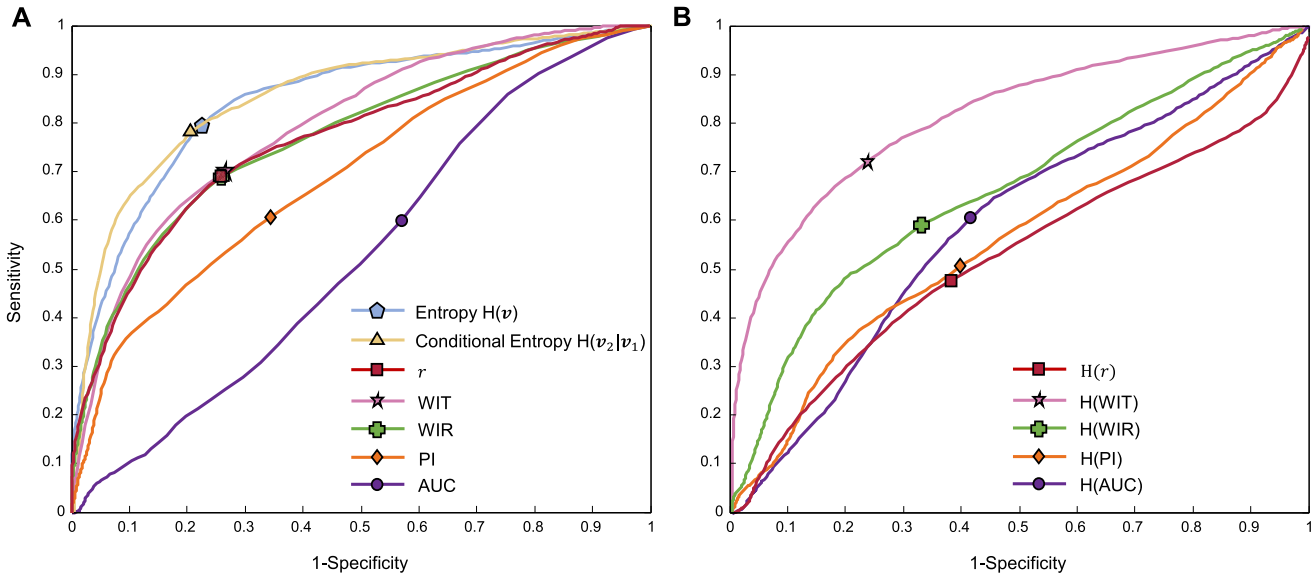

Fig. 8. Receiver-Operating-Characteristic (ROC) curves for the classification performance of the proposed Entropy [H▷$\mathcal{E}$◁] and Conditional Entropy [H▷$\mathcal{E}_2|\mathcal{E}_1$◁] of velocity fields ($R$=0.9 mm, N_b=12 bins), against those obtained with spatio-temporal IDC correlation (r), wash-in time (WIT), wash-in rate (WIR), peak intensity (PI) and the area under the IDC (AUC) as parameters (A). The ROC curves obtained when using the entropy [H(·)] of these parameters are shown in (B).

predictive value. These statistics are always the highest for either Entropy or Conditional Entropy.

In addition to this, the results for ROI-based classification are presented in Table III, by taking the mean value of each parameter in the ROI. The highest sensitivity, specificity, negative predictive value and positive predictive value are reached by the Conditional Entropy of the velocity fields.

TABLE II

PIXEL-BASED CLASSIFICATION PERFORMANCE IN TERMS OF SENSITIVITY (SEN), SPECIFICITY (SPC), NEGATIVE PREDICTIVE VALUE (NPV), POSITIVE PREDICTIVE VALUE (PPV), AND RECEIVER-OPERATING-CHARACTERISTICS (ROC) CURVE AREA. FOR BOTH ENTROPY [$H(V)$] AND CONDITIONAL ENTROPY [$H(V_2|V_1)$], THE RESULTS WITH SETTINGS THAT YIELD THE HIGHEST ROC CURVE AREA (SEE FIGURE 4) ARE GIVEN. AS A REFERENCE, OTHER RELEVANT PARAMETERS FOR DCE-US QUANTIFICATION PROPOSED IN THE LITERATURE ARE ALSO GIVEN, ALONG WITH THEIR SPATIAL HETEROGENEITY BASED ON ENTROPY

Parameter	SEN [%]	SPC [%]	NPV [%]	PPV [%]	ROC curve area	p-value
Entropy $H(V)$	79.8	78.4	79.5	78.7	0.849	$\ll 0.01$
Conditional Entropy $H(V_2\|V_1)$	77.9	78.9	78.1	78.7	0.854	$\ll 0.01$
Spatiotemporal correlation r	68.6	74.5	70.4	72.9	0.763	$\ll 0.01$
Wash-in time	69.2	74.1	70.6	72.7	0.786	$\ll 0.01$
Wash-in rate	68.5	74.3	70.2	72.7	0.759	$\ll 0.01$
Peak-intensity	60.5	65.7	62.4	63.8	0.682	$\ll 0.01$
AUC	59.7	43.1	51.7	51.2	0.513	0.58
Entropy of spatiotemporal correlation r	47.8	62.1	54.3	55.8	0.522	0.63
Entropy of wash-in time	72.1	76.7	73.3	75.5	0.816	$\ll 0.01$
Entropy of wash-in rate	59.0	67.2	62.1	64.3	0.646	$\ll 0.01$
Entropy of Peak-intensity	50.8	60.4	55.1	56.2	0.549	0.23
Entropy of AUC	60.6	58.6	59.8	59.4	0.590	0.09

TABLE III

REGION-BASED CLASSIFICATION PERFORMANCE IN TERMS OF SENSITIVITY (SEN), SPECIFICITY (SPC), NEGATIVE PREDICTIVE VALUE (NPV) AND POSITIVE PREDICTIVE VALUE (PPV) ARE GIVEN FOR THE OPTIMAL THRESHOLD. THE TRUE POSITIVES (TP), TRUE NEGATIVES (TN), FALSE POSITIVES (FP) AND FALSE NEGATIVES (FN) ARE ALSO SHOWN, ALONG WITH THE OVERALL ACCURACY

Parameter	SEN [%]	SPC [%]	NPV [%]	PPV [%]	TP	TN	FP	FN	Accuracy [%]
Entropy $H(V)$	81	79	80	80	43	41	11	10	80
Conditional Entropy $H(V_2\|V_1)$	81	83	81	83	43	43	9	10	82
Spatiotemporal correlation r	64	83	69	68	34	43	9	19	73
Wash-in time	70	79	72	77	37	41	11	16	74
Wash-in rate	72	65	69	68	38	34	18	15	69
Peak-intensity	62	62	62	62	33	32	20	20	62
AUC	49	62	54	57	26	32	20	27	55
Entropy of spatiotemporal correlation r	49	67	57	61	26	35	17	27	58
Entropy of wash-in time	76	83	77	82	40	43	9	13	79
Entropy of wash-in rate	62	65	63	65	33	34	18	20	64
Entropy of Peak-intensity	45	73	57	63	24	38	14	29	59
Entropy of AUC	66	60	63	63	35	31	21	18	63

V. CONCLUSIONS AND DISCUSSION

In this paper, we presented a method for the estimation and statistical characterization of flow vector fields from clinically acquired DCE-US data. By employing time-delay estimation in combination with least squares minimization, the proposed method enables estimation of the in-plane flow vector fields of perfused microvasculature, after which histogram-based measures of heterogeneity are extracted: the vector field's Entropy and Conditional Entropy.

Both Entropy and Conditional Entropy estimates yielded higher values in malignant areas. The typical examples of benign and malignant probability density functions shown in Figure 3 indeed display a broader distribution of velocity vectors for the malignant case. Qualitatively, this can also be observed from Figure 2, where an example of the obtained flow vector fields is shown for one DCE-US plane. The complexity of the flow patterns is noticeable in the area corresponding to the tumor location. Moreover, one can recognize multiple field "sources" and "sinks". We hypothesize that these coincide with feeding and draining vessels that enter the imaging plane and perfuse the area through the microvasculature. The Entropy and Conditional Entropy of the fields both display elevated values in malignant regions; a finding that is confirmed by the quantitative analysis. When trialled on a set of 24 patients, Entropy and Conditional Entropy are significantly higher in malignant pixels as compared to benign

pixels ($p \ll 0.01$). Presuming that these features reflect the heterogeneity of contrast-agent flow patterns, this result is in line with previous observations on the heterogeneous nature of blood flow in tumors [11].

The pixel-based classification performance for detecting prostate cancer was expressed in terms of the ROC curve area. On the entire dataset, the proposed parameters outperformed all other evaluated DCE-US features, and both resulted in a should be an ROC curve area of approximately 0.85. Spatiotemporal correlation, WIR and WIT yielded lower performances (ROC curve areas of 0.76, 0.76, and 0.79, respectively), followed by the amplitude-based peak-intensity (ROC curve area of 0.68) and area under the IDC (ROC curve area of 0.51). The latter aims to reflect the level of perfusion based on the IDC integral, but is hampered by the ambiguity between blood fractional volume and velocity, as well as by the dependency on ultrasound pressure and attenuation.

In this work, assessement of heterogeneity of flow was proposed by calculating the entropy of UCA velocity fields. In addition, we evaluated the entropy of other DCE-US features. Of these, only WIT entropy and WIR entropy display a significant ($p \ll 0.01$) difference between malignant and benign pixels. As expected, the mean WIR entropy was indeed higher for malignant pixels, since WIR is proportional to flow. Its classification performance is limited however (sensitivity and specificity of 62.3% and 65.4%, respectively). On the other hand, the mean WIT entropy is significantly lower for the malignant distribution, reaching a test sensitivity and specificity of 72.1% and 76.7%, respectively (see Table II). This observed local similarity in wash-in times may be a direct consequence of the inverse proportionality of WIT to flow velocity: heterogeneities in flow cause reduced variations in WIT for high flows.

Interestingly, pixel-based classification performance of velocity field Entropy and Conditional Entropy monotonically increases when excluding pixels that suffer from a low signal to noise ratio (SNR). This most likely leads to exclusion of wrongly estimated velocity vectors, as estimation of time-delays between IDCs becomes increasingly difficult for higher noise levels. Therefore, the development of a time-delay estimation procedure that is more robust in the presence of the low SNR conditions observed in DCE-US measurements is part of future work. In line with this, dedicated maximum likelihood estimators based on the particular noise statistics of DCE-US (Rayleigh distribution) may be exploited.

The frame rate of the imaging system plays a primordial role in the estimation of time-delays. In this work, the selected rate of 10 Hz was sufficient to reach the required velocity resolution for the Entropy analysis: the histogram bin width (0.167 mm/s). The latter is approximately equal to the error standard deviation of the estimated velocity magnitudes obtained in the *in-silico* validation (Appendix A).

The Entropy and Conditional Entropy are determined by estimating the probability distributions of the vector fields using bivariate histograms. The histogram estimator approximates the true density from the data using rectangular bins. The probability for a value to fall within such a bin is calculated based on the incidence of these values in the dataset. The larger the dataset (kernel size) on which the density is estimated, the higher the accuracy of this probability estimate. As a consequence, the spatial resolution of the analysis decreases. The required amount of samples depends on the amount of histogram bins. Choosing a smaller number of bins requires less samples to effectively fill those bins, but deteriorates the resolution of the histogram. This realization touches upon a fundamental trade-off. In our test set, the highest ROC curve area was attained using 12 bins in both directions.

An alternative to the histogram estimator is the kernel density estimator [40]. In this case, the probability distribution is represented by a mixture of kernels (e.g., a Gaussian) that have a certain adjustable bandwidth. Although this approach can yield a smooth estimate of the density function, it is computationally more demanding. The methodology presented in the present paper requires estimating one probability distribution per pixel for Entropy, and N_b^2 probability distributions per pixel for Conditional Entropy. Hence, we chose to employ the fast histogram estimator as opposed to the kernel density estimator.

The validity of the results presented in this work is hampered by the limitations of the quantitative validation procedure. First of all, histological assessment of Haematoxylin & Eosin stained prostate specimens is based on the level of cell-differentiation, whereas the developed methods are aimed at detecting angiogenesis. Hence, not all malignantly labelled time-intensity curves are necessarily obtained from angiogenic vasculature. It would therefore be interesting to validate the methods presented in this work with stains of the endothelial marker CD31, or the angiogensis-stimulating vascular endothelial growth factor (VEGF). Secondly, the registration procedure has some pitfalls. The ultrasound imaging planes are in general not parallel to the histology slices, as specific pathological guidelines constrain the dissection procedure. Finally, the performance is biased towards large tumors and those that are consistent through multiple slices. This is a consequence of the infeasibility of drawing reliable regions-of-interest for small and scattered tumors, given the adopted registration procedure.

The adopted time-delay estimator relies on the assumption that IDCs show a strong local similarity in shape. Violations of this assumption impact the estimation accuracy. In case of high local bolus dispersion or diffusion, a model-based transit time estimator that incorporates the IDC shape alteration (e.g. the local density random walk model) may be employed [41].

The velocity field estimator described in (5) uses the time-delay estimates obtained at a set of pixels to infer a local dominant propagation vector. As such, the attained velocity vector represents the macroscopic contribution of flows originating from all vessels in the final resolution cell. To test the performance of the estimator given such macroscopically measured flows, we performed a simple *in-silico* experiment, in which the propagation of a UCA bolus through an intermediately sized branching structure was simulated. The introduction of random walk motion in this propagation model facilitated the generation of microscopic UCA particle trajectories, that

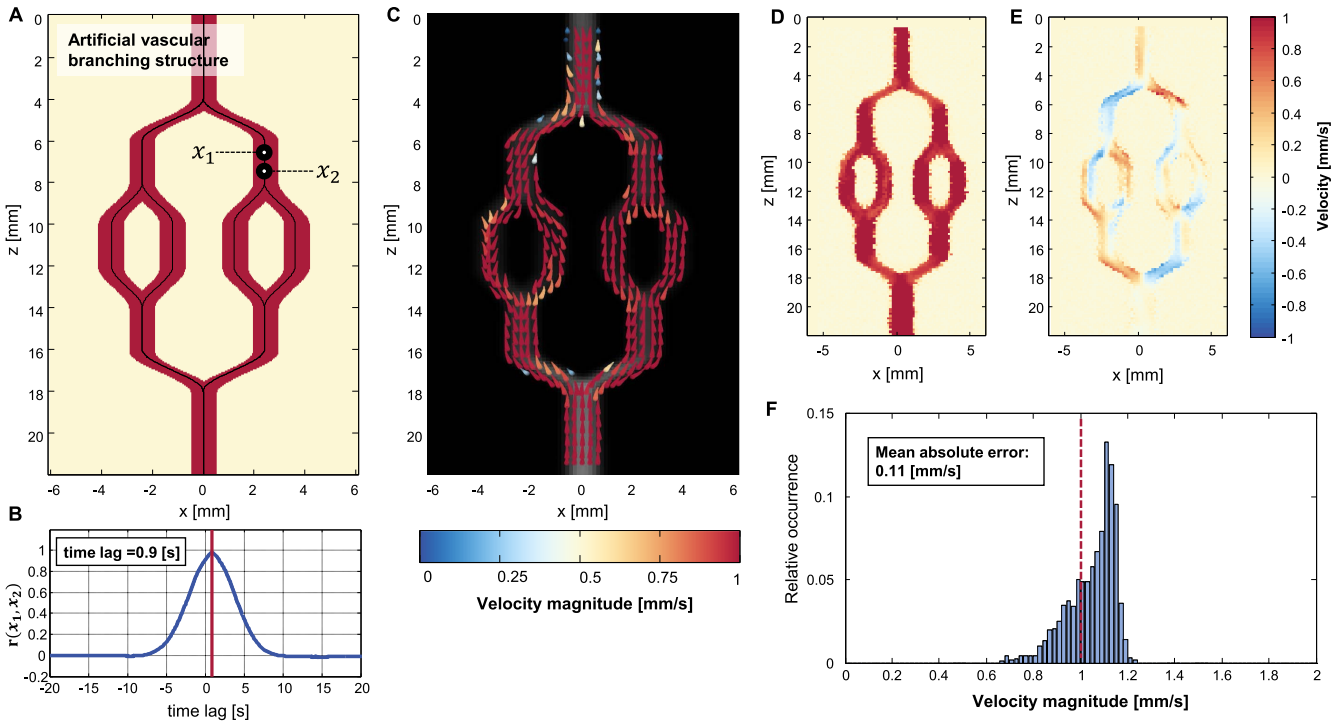

Fig. 9. *In-silico* validation of velocity vector field estimation. The artificial branching structure is shown (A), along with the cross correlation function of the time-intensity curves obtained at two locations x_1 and x_2 (B). The estimated velocity vector field mapped on the maximum intensity projection is given in (C). The axial and lateral velocity components are shown in (D) and (E), respectively. A histogram of the obtained velocity magnitude estimates within the structure is given in (F).

lead to macroscopic bolus dispersion. Although this simple experiment yielded promising results, its performance on a physiologically more realistic model (*in-silico* or *in-vitro*) of flow trough the capillary network of a tumor could be studied as a topic of future work. Given such a model, an extensive validation of the proposed entropy measures may be performed.

The presented method is applied to 2D DCE-US data. Hence, out of plane flows affect the velocity estimates and lead to an ambiguity between the elevational orientation and magnitude of the velocity vector. In fact, the lateral and axial velocity vector components are the projections of the true 3D velocity vector onto the imaging plane. With this in mind, heterogeneity in the elevational component of this vector within the kernel would be reflected by its estimated magnitude. As a result, it would contribute to the estimated Entropy.

Recently, 4D DCE-US imaging systems have been introduced. Such systems facilitate the acquisition of 3D volumes over time and hence permit an analysis that incorporates the full 3D spatial information [42]. One can envisage computing 3D velocity vector fields by performing the time-delay estimation procedure on a set of voxels that are distributed in 3D space. The spatial entropy analysis can then be implemented based on a spherical kernel in combination with trivariate probability density estimation. The added dimension comes at the price of a reduced frame rate of the ultrasound data, which impairs the temporal resolution of the cross-correlation based delay estimator employed in this paper. Nevertheless, contrast-agent bolus injections produce time intensity curves that contain dominantly low frequency content (<0.5 Hz) [42]. Hence the required phase information is retained, even at the low frame rates achieved by 4D systems. The extension of the proposed method to 4D DCE-US, along with the development of algorithms that provide high-resolution time-delay estimation in these systems, will be part of future work. Additionally, the possiblity of staging the severity of lesions in terms of the Gleason grade can be investigated.

The proposed time-delay based approach can be applied to DCE-US recordings of any perfused organ to resolve flow patterns with magnitudes that can be well below 1 mm/s, such as those found in tumor arterioles and capillaries [43]. As such, this provides a key advantage with respect speckle-tracking based methods, which are designed to image the relatively high flows found in arteries and the heart, and suffer from the severe speckle decorrelation that results from UCAs moving through the microvasuclature as opposed to a large blood pool.

Appendix I
In-Silico Validation of Vector Fields

In this section, the vector velocity field estimator is validated using an *in-silico* experiment in which the 2D transport of particles (microbubbles) through an artificial branching (vascular) structure was simulated. For this purpose, particles were propagated through the structure with a given velocity, comprising a deterministic flow plus an additional Gaussian process noise component. The former simulates pure convection, whereas the latter served as a model for diffusion. Particles were bound to stay within 0.5 mm of the central axis (vessel radius). The

amount of particles was 2000. The velocity magnitude was set to 1 mm/s.

The ultrasound acquisition of this process was simulated by modelling the scanner's point spread function as a bivariate Gaussian, with standard deviations that are dependent on the axial (0.156 mm) and lateral ($0.142 + 0.0054 \times z$ mm) resolution, where z is the imaging depth. These numbers are selected based on measurements of the speckle-grain dimensions as a function of imaging depth for the C10-3v transrectal endfiring ultrasound probe in combination with the Philips iU22 scanner [44]. The frame rate was set to 10 Hz, and the pixel spacing was 0.15 mm.

The velocity vector fields were estimated according to the procedure described in section II-E. The adopted values for N and R are 8 and 0.5 mm, respectively. Figure 9 displays the observed maximum intensities of all the ultrasound time-intensity curves (maximum intensity projection) along with the velocity vector estimates in pixels with a peak-intensity greater than 10% of the maximum intensity. The estimated velocities in both the axial and lateral direction as well as the histogram of velocity magnitudes within the branching structure are also given. The mean absolute error of the velocity magnitudes is 0.11 mm/s, and the standard deviation of the error is 0.17 mm/s.

REFERENCES

[1] *Cancer Facts Figures*, Amer. Cancer Soc., Atlanta, GA, USA, 2015.

[2] D. F. Gleason, "Histologic grading of prostate cancer: A perspective," *Human Pathol.*, vol. 23, no. 3, pp. 273–279, 1992.

[3] K. A. Roehl, J. A. V. Antenor, and W. J. Catalona, "Serial biopsy results in prostate cancer screening study," *J. Urol.*, vol. 167, no. 6, pp. 2435–2439, 2002.

[4] J. E. Thompson *et al.*, "Multiparametric magnetic resonance imaging guided diagnostic biopsy detects significant prostate cancer and could reduce unnecessary biopsies and over detection: A prospective study," *J. Urol.*, vol. 192, no. 1, pp. 67–74, 2014.

[5] S. Vourganti *et al.*, "Multiparametric magnetic resonance imaging and ultrasound fusion biopsy detect prostate cancer in patients with prior negative transrectal ultrasound biopsies," *J. Urol.*, vol. 188, no. 6, pp. 2152–2157, 2012.

[6] J. Folkman, "Role of angiogenesis in tumor growth and metastasis," *Seminars Oncol.*, vol. 29, no. 2, pp. 15–18, 2002.

[7] M. K. Brawer, "Quantitative microvessel density: A staging and prognostic marker for human prostatic carcinoma," *Cancer*, vol. 78, no. 2, pp. 345–349, 1996.

[8] N. Weidner, P. R. Carroll, J. Flax, W. Blumenfeld, and J. Folkman, "Tumor angiogenesis correlates with metastasis in invasive prostate carcinoma," *Amer. J. Pathol.*, vol. 143, no. 2, pp. 401–409, 1993.

[9] D. Hanahan and R. A. Weinberg, "The hallmarks of cancer," *Cell*, vol. 100, no. 1, pp. 57–70, 2000.

[10] J. Chang and J. Erler, "Hypoxia-mediated metastasis," in *Tumor Microenvironment Cellular Stress*. New York, NY, USA: Springer, 2014, pp. 55–81.

[11] R. J. Gillies, P. A. Schomack, T. W. Secomb, and N. Raghunand, "Causes and effects of heterogeneous perfusion in tumors," *Neoplasia*, vol. 1, no. 3, pp. 197–207, 1999.

[12] D. Cosgrove, "Angiogenesis imaging–ultrasound," *Br. J. Radiol.*, vol. 76, no. 1, p. S43, 2014.

[13] G. J. Lueck, T. K. Kim, P. N. Burns, and A. L. Martel, "Hepatic perfusion imaging using factor analysis of contrast enhanced ultrasound," *IEEE Trans. Med. Imag.*, vol. 27, no. 10, pp. 1449–1457, Oct. 2008.

[14] D. Cosgrove and N. Lassau, "Imaging of perfusion using ultrasound," *Eur. J. Nucl. Med. Molecular Imag.*, vol. 37, no. 1, pp. 65–85, 2010.

[15] K. Wei, E. Le, J.-P. Bin, M. Coggins, J. Thorpe, and S. Kaul, "Quantification of renal blood flow with contrast-enhanced ultrasound," *J. Amer. College Cardiol.*, vol. 37, no. 4, pp. 1135–1140, 2001.

[16] T. P. Gauthier, M. A. Averkiou, and E. L. Leen, "Perfusion quantification using dynamic contrast-enhanced ultrasound: The impact of dynamic range and gain on time–intensity curves," *Ultrasonics*, vol. 51, no. 1, pp. 102–106, 2011.

[17] T. P. Gauthier, M. Chebil, P. Peronneau, and N. Lassau, "*In vitro* evaluation of the impact of ultrasound scanner settings and contrast bolus volume on time–intensity curves," *Ultrasonics*, vol. 52, no. 1, pp. 12–19, 2012.

[18] M.-X. Tang *et al.*, "Quantitative contrast-enhanced ultrasound imaging: A review of sources of variability," *Interface Focus*, vol. 1, no. 4, pp. 520–539, 2011.

[19] M. Cao, Y. Liang, C. Shen, K. D. Miller, and K. M. Stantz, "Developing DCE-CT to quantify intra-tumor heterogeneity in breast tumors with differing angiogenic phenotype," *IEEE Trans. Med. Imag.*, vol. 28, no. 6, pp. 861–871, Jun. 2009.

[20] A. Jackson, J. P. O'Connor, G. J. Parker, and G. C. Jayson, "Imaging tumor vascular heterogeneity and angiogenesis using dynamic contrast-enhanced magnetic resonance imaging," *Clin. Cancer Res.*, vol. 13, no. 12, pp. 3449–3459, 2007.

[21] P. Frinking, L. Mercier, N. Rognin, M. Arditi, F. Tranquart, and M. Schneider, "Real-time contrast-enhanced ultrasound parametric imaging in prostate," in *Proc. 15th Eur. Symp. Ultrasound Contrast Imag.*, 2010, pp. 40–49.

[22] G. Barrois, A. Coron, and S. L. Bridal, "Detection of early therapeutic response with dynamic contrast enhanced ultrasound using a perfusion clustering algorithm," in *Proc. IEEE Int. Ultrason. Symp.*, Sep. 2014, pp. 1754–1757.

[23] M. P. J. Kuenen, M. Mischi, and H. Wijkstra, "Contrast-ultrasound diffusion imaging for localization of prostate cancer," *IEEE Trans. Med. Imag.*, vol. 30, no. 8, pp. 1493–1502, Aug. 2011.

[24] M. P. J. Kuenen, T. A. Saidov, H. Wijkstra, J. D. de L. Rosette, and M. Mischi, "Correspondence—Spatiotemporal correlation of ultrasound contrast agent dilution curves for angiogenesis localization by dispersion imaging," *IEEE Trans. Ultrason., Ferroelect., Freq. Control*, vol. 60, no. 12, pp. 2665–2669, Dec. 2013.

[25] P. Saffman, "A theory of dispersion in a porous medium," *J. Fluid Mech.*, vol. 6, no. 3, pp. 321–349, 1959.

[26] G. A. Taylor, "Dispersion of soluble matter in solvent flowing slowly through tube," *Proc. R. Soc. Lond. A, Math. Phys. Sci.*, vol. 219, pp. 186–203, Aug. 1953.

[27] J. M. Hudson, R. Karshafian, and P. N. Burns, "Quantification of flow using ultrasound and microbubbles: A disruption replenishment model based on physical principles," *Ultrasound Med. Biol.*, vol. 35, no. 12, pp. 2007–2020, 2009.

[28] M. Krix, F. Kiessling, N. Farhan, K. Schmidt, J. Hoffend, and S. Delorme, "A multivessel model describing replenishment kinetics of ultrasound contrast agent for quantification of tissue perfusion," *Ultrasound Med. Biol.*, vol. 29, no. 10, pp. 1421–1430, 2003.

[29] M. O. Hill, "Diversity and evenness: A unifying notation and its consequences," *Ecology*, vol. 54, no. 2, pp. 427–432, 1973.

[30] C. E. Shannon, "A mathematical theory of communication," *ACM SIGMOBILE Mobile Comput. Commun. Rev.*, vol. 5, no. 1, pp. 3–55, 2001.

[31] N. D. Jong, P. J. Frinking, A. Bouakaz, and F. J. T. Cate, "Detection procedures of ultrasound contrast agents," *Ultrasonics*, vol. 38, no. 1, pp. 87–92, 2000.

[32] R. Montironi, T. V. D. Kwast, L. Boccon-Gibod, A. Bono, and L. Boccon-Gibod, "Handling and pathology reporting of radical prostatectomy specimens," *Eur. Urol.*, vol. 44, no. 6, pp. 626–636, 2003.

[33] R. Bourne, *Fundamentals of Digital Imaging in Medicine*. New York, NY, USA: Springer, 2010.

[34] G. Barrois, A. Coron, T. Payen, A. Dizeux, and L. Bridal, "A multiplicative model for improving microvascular flow estimation in dynamic contrast-enhanced ultrasound (DCE-US): Theory and experimental validation," *IEEE Trans. Ultrason., Ferroelect., Freq. Control*, vol. 60, no. 11, pp. 2284–2294, Nov. 2013.

[35] M. P. J. Kuenen, I. H. F. Herold, H. H. M. Korsten, J. J. M. C. H. de la Rosette, H. Wijkstra, and M. Mischi, "Maximum-likelihood estimation for indicator dilution analysis," *IEEE Trans. Biomed. Eng.*, vol. 61, no. 3, pp. 821–831, Mar. 2014.

[36] A. K. Nandi, "On the subsample time delay estimation of narrowband ultrasonic echoes," *IEEE Trans. Ultrason., Ferroelect., Freq. Control*, vol. 42, no. 6, pp. 993–1001, Nov. 1995.

[37] M. Stücker, V. Baier, T. Reuther, K. Hoffmann, K. Kellam, and P. Altmeyer, "Capillary blood cell velocity in human skin capillaries located perpendicularly to the skin surface: Measured by a new laser Doppler anemometer," *Microvascular Res.*, vol. 52, no. 2, pp. 188–192, 1996.

[38] C. Strouthos, M. Lampaskis, V. Sboros, A. McNeilly, and M. Averkiou, "Indicator dilution models for the quantification of microvascular blood flow with bolus administration of ultrasound contrast agents," *IEEE Trans. Ultrason., Ferroelect., Freq. Control*, vol. 57, no. 6, pp. 1296–1310, Jun. 2010.

[39] W. H. Kruskal and W. A. Wallis, "Use of ranks in one-criterion variance analysis," *J. Amer. Statist. Assoc.*, vol. 47, no. 260, pp. 583–621, 1952.

[40] Z. I. Botev, J. F. Grotowski, and D. P. Kroese, "Kernel density estimation via diffusion," *Ann. Statist.*, vol. 38, no. 5, pp. 2916–2957, 2010.

[41] R. J. V. Sloun, L. Demi, A. W. Postema, J. J. D. L. Rosette, H. Wijkstra, and M. Mischi, "Ultrasound-contrast-agent dispersion and velocity imaging for prostate cancer localization," *Med. Image Anal.*, vol. 35, pp. 610–619, Jan. 2017.

[42] S. G. Schalk *et al.*, "4-D spatiotemporal analysis of ultrasound contrast agent dispersion for prostate cancer localization: A feasibility study," *IEEE Trans. Ultrason., Ferroelect., Freq. Control*, vol. 62, no. 5, pp. 839–851, May 2015.

[43] M. Leunig *et al.*, "Angiogenesis, microvascular architecture, microhemodynamics, and interstitial fluid pressure during early growth of human adenocarcinoma LS174T in SCID mice," *Cancer Res.*, vol. 52, no. 23, pp. 6553–6560, 1992.

[44] M. P. J. Kuenen, T. A. Saidov, H. Wijkstra, and M. Mischi, "Contrast-ultrasound dispersion imaging for prostate cancer localization by improved spatiotemporal similarity analysis," *Ultrasound Med. Biol.*, vol. 39, no. 9, pp. 1631–1641, 2013.